# Seamless Hyperspectral High Spatial Mosaic Derived From Chang'E-1 IIM

**Yunzhao Wu, Z. C. Wang, X. Tang, X. M. Zhang, Y. Chen, and W. Cai**
School of Geographic and Oceanographic Sciences, Nanjing University, Nanjing 210023, China .
Email: wu@nju.edu.cn

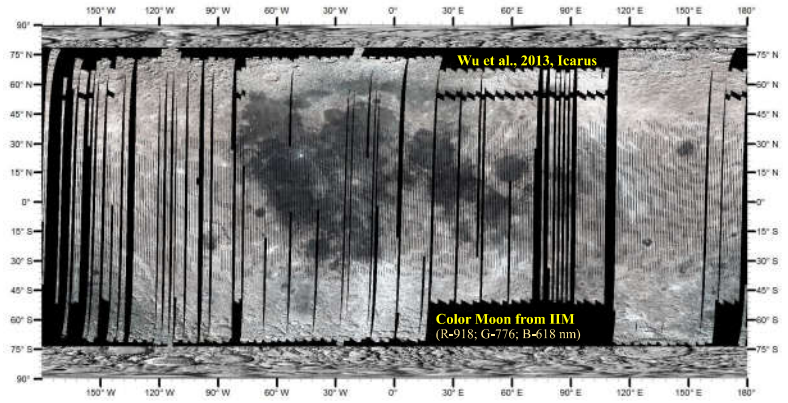


Fig. 1. Seamless hyperspectral and high spatial mosaic of IIM using the method described in [1] with 151.6 px/d.

## Introduction and Purpose

- We finished the seamless hyperspectral and high spatial resolution mosaic (Fig. 1) for IIM reflectance data at standard geometry (30°, 0°, 30 °) which were processed using the pipeline described in [1].
- **Users are welcome to contact us for these products including both mosaic and individual orbital**.
- The mosaic is 26 bands (522-918 nm) because the first 5 bands and the last band were removed due to the low SNR. The size is 122 Gb for the mosaic and 120 Gb for all the individual orbits.
- This seamless product can have several uses such as minerals, elements and geology, comparison of lunar irradiance model and absolute reflectance, calibration for Earth observation sensors and separation of basaltic units, etc.

## Introduction to IIM

- The Chang' E-1 Interference Imaging Spectrometer (IIM) is a sagnac-based spatially modulated Fourier transform imaging spectrometer (Table 1 and Fig.2).

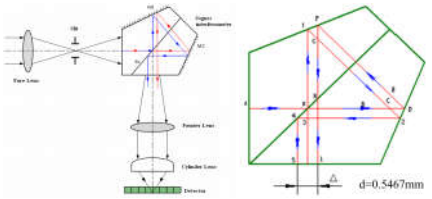


Fig. 2. Schematic of the IIM. The lunar surface is imaged onto a slit aperture using the Fore Lens. Light emerging from the slit is sheared by the Sagnac interferometer and collimated by the Fourier lens. The cylindrical lens reimages the spatial axis of the slit onto the detector array.

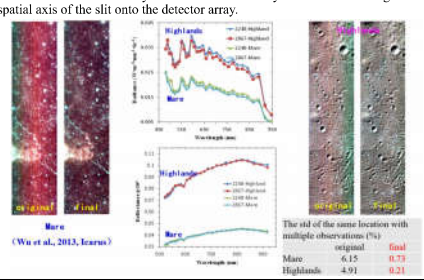


| Table 1 The performance characteristics of IIM | |
|---|---|
| Swath width | 25.6 km |
| Imaging coverage | Between 75°S and 75°N |
| Digital level | 12 bit |
| Pixel No. | 128*128 (256*256 after 2*2 combination) |
| Spectral range | 480-960 nm |
| Spectral resolution | 325.5 $cm^{-1}$ |
| Space resolution | 200 m (orbit altitude=200km) |
| Spectral channels | 32 bands |
| Modulated Transferring Function | 0.51 (snapshot) |
| SNR | 375 (snapshot) |
| F/# | F/2.4 |
| Instantaneous-field-of-view (IFOV) | 1 milliradian |
| Slit width | 0.6 milliradian |
| data compression ratio | No |
| Apodization | No |
| Electronic gain | 1 (typical used), 1.5 and 2 |
| Exposure time | 140 ms (typical used) and |
| Frame rate | 7.1 FPS (typical ) and 14.2 FPS |
| Data rate | 1363 kbps |
| read noise | No measurement |
| Interferogram sampling mode | double sided sampling |
| fringe visibility | 64%@543.5nm |
| out-of-band rejection | <1% |

Fig. 3. The bad points, stripes and inhomogeneity were moved (see next Section below and reference 1). For the final products, the IIM reflectance of the same location with multiple observations match very well with std less

## Calibration and Photometric correction of IIM

- The lab spectral calibration shows the spectral position accuracy of 0.04 nm @543 nm to 2.48 nm@831 nm. The full FOV radiometric calibration shows average uncertainty of 3.56%. The IIM signal chain is linear over most of the range (<1%) with a small nonlinearity at the lowest signal levels (2.5%). IIM is very stable because it has no mobile apparatus and with good thermal protection
- To build the photometric model, the Moon was calssified into 4 classess (Fig.4: very bright rays, mature highlands, low-Fe basalts, and high-Fe basalts), perhaps the most classes of the existing models. The photometric correction was applied to each pixel by applying suitable model pixel-by-pixel.
- The usual in-flight flat-field correction often removes the cross-track photometric signal. We provided a new method for decoupling the combined effects of the photometry and non-uniformity of detector response along the cross-track. The orbits used for deriving the correction factor are systematically distributed with respect to zero beta angle, the photometric effects can be counteracted by stacking all the lines (Fig. 5).
- Previously, the bad pixels were detected commonly with only a single band. We used multiple bands to detect bad pixels with spectral angle mapping . Subsequently the bad pixels were replaced by the average value of their immediate neighbors.

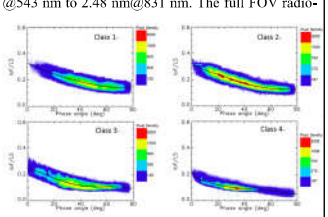


Fig. 4. The phase functions of the four classes@757 nm

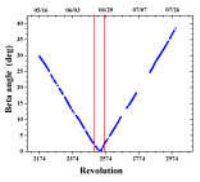


Fig. 5. The relation between the β angle and the IIM revolution Φ.The orbits within the range of the two red lines are used to calculate the in-flight flat-field image.

## Seamless images and absolute reflectance of the Moon

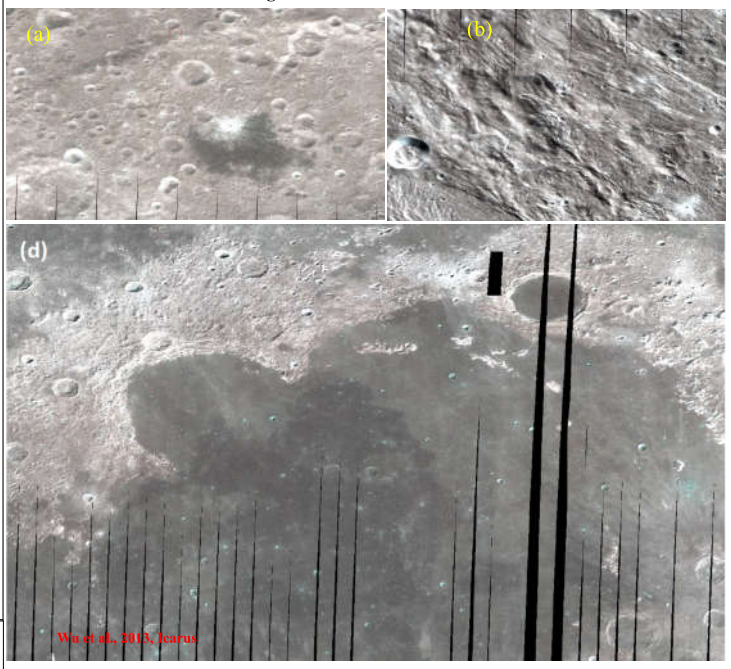


- Fig. 6. Examples of hyperspectral mosaics of IIM for north hemisphere (a), south hemisphere (b) and northwest Imbrium (d). The boundaries between adjacent orbits are invisible. This also demonstrates the quality of our photometric model.

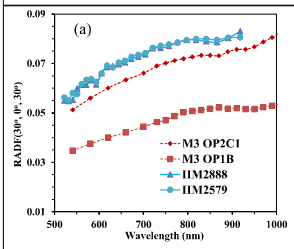


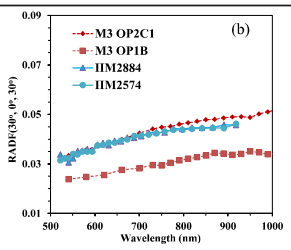


Fig. 7. The IIM reflectance comparison of the same location with multiple observations and other data. (a) The brightest area in Sinus Iridum. (b) The darkest area in Sinus Iridum. Other areas are shown in the legend.

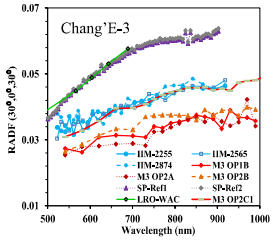


- IIM and OP2C $M^3$ match well, and both are consistent with the CE-3 in situ reflectance, which has the onboard calibration panel.
- The reflectance measured in the laboratory is the largest.

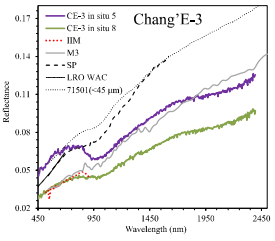


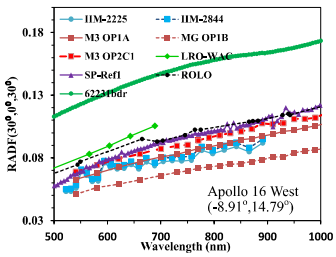


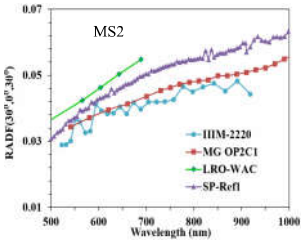


1.IIM reflectance of the same location with multiple observations match very well with std less than 0.01, which also demonstrates the quality of our lunar model.
2.All the orbital reflectance is much smaller than the Apollo sample reflectance.
3.LRO WAC reflectance is the largest and most red among all the orbital reflectance. Then is SP.
4.The reflectance of IIM is much larger than the OP1B $M^3$ reflectance and comparable to OP2C1 $M^3$ reflectance.
5.The IIM reflectance was calculated using the solar irradiance spectra ATLAS 3 [3], which was the only one measured outside the Earth' atmosphere during low solar activity.

## References

[1] Wu, Y. Z. et al. (2013) *Icarus*, 222, 283-295. [2] Wu, Y. Z. et al. (2012) *JGR*, 117, 1-23. [3] Thuillier, G. et al. (2003) *Geophys. Monogr.*, 141, 171-194. [4] Yokota, Y. et al. (2011) *Icarus*, 215, 639-660. [5] Besse, S. et al. (2013) *Icarus*, 222, 229-242. [6] Wagner, R. V. et al. (2015) *LPS XLVI*, abstract #1473.